Electronic Supplementary Material (ESI) for CrystEngComm.


# Sodium Tantalates: Monitoring Crystallization via *in situ* Total X- Ray Scattering

Ezgi Onur Şahin,[1] Siyuan Zhang,[2] Christina Scheu,[2] Claudia Weidenthaler[1*]

[1]Max-Planck-Institut für Kohlenforschung, Diffraction and Spectroscopy, Kaiser-Wilhelm-Platz 1, 45470 Mülheim an der Ruhr (Germany)

[2]Max-Planck-Institut für Eisenforschung GmbH, Nanoanalytics and Interfaces, Max-Planck-Straße 1, 40237 Düsseldorf (Germany)

## Supporting Information

## Experimental

### Preparation procedure

The preparation method[1] involves injection of 448 µL tantalum(V) ethoxide [$Ta(OEt)_5$, 99.98%, Sigma Aldrich, CAS: 6074-84-6] as one of the metal oxide precursors predispersed in 10 mL methanol (MeOH, Sigma Aldrich, CAS: 67-56-1) into a mixture of 360 mL deionized water and in a glass beaker. The container of $Ta(OEt)_5$ was washed with 10 mL MeOH and this part was also added to the reaction solution. 104 mg sodium ethoxide (NaOEt, 95%, Sigma Aldrich, CAS: 141-52-6) was injected to 20 mL MeOH and dispersed using ultrasonic bath and immediately poured into the reaction solution.

The amounts of the precursors added were calculated aiming 1 $g \cdot L^{-1}$ $NaTaO_3$ catalyst in the end. The reaction mixture was stirred (using a glass stirring rod connected to the motor at 450 rpm) for 2 h under continuous Ar purging (via a PTFE tubing sent inside the solution). In order to have dry powder samples, the sediments were separated from the suspensions by decanting off the liquid part. The remaining parts were dried overnight at 60 °C in an oven to obtain $Na_xTa_yO_z$. These samples are studied extensively including the *in situ* temperature-dependent experiments in the present work.

### Total scattering experiments

*In situ* temperature-dependent total scattering experiments were performed on $Na_xTa_yO_z$ at beamline P02.1 at PETRA III, Deutsches Elektronen-Synchrotron (DESY) [energy: 60 keV (λ= 0.20723 Å); detector: Perkin Elmer XRD 1621; sample to detector distance: 250.88 mm; $Q_{min}$ = 0.4 $Å^{-1}$ and $Q_{max,\ instrumental}$ = 34.2 $Å^{-1}$, beam size: 1 x 1 mm]. Powder samples were packed in both ends open quartz capillaries (length 100 mm, inner diameter 0.9 mm, wall thickness 0.15 mm) ensuring a few centimeters of sample length. The capillaries mounted on the custom-made cell were heated at a rate of 10 $K \cdot min^{-1}$ using a hot air blower. The temperature was calibrated based on the trend obtained from the reading of the thermocouple inserted inside the empty quartz capillary heated in the same way as the samples. The temperature calibration curve and temperature vs. time curve for the data used in the local structure analysis in the present work (described as the main set of experiments) are given in Fig. S1 and Fig. S2. During heating, the

powder was kept under synthetic air with a flow of 5 mL·min$^{-1}$. Data were collected at 30 °C and in temperature steps of 10 °C between 500 and 700 °C. The maximum temperature of the experiments were limited by the maximum energy obtained by the hot air blower. The data collection time per frame was 5 min. The DAWN software package was used to integrate scattering data.[2] PDFs were generated ($q_{max}$ = 22 Å$^{-1}$) using PDFgetX3[3] implemented in the xPDFsuite,[4] simulated ($q_{max}$ = 22 Å$^{-1}$, ADPs= 0.003, delta2=1.0, $Q_{damp}$= 0.0375 Å$^{-1}$, $Q_{broad}$= 4.067e-06 Å$^{-1}$) and was fitted using PDFgui.[5]

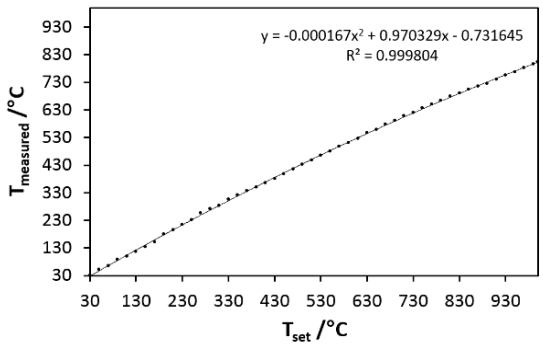


**Fig. S1** Temperature calibration curve used for setting the temperature for the hot air blower

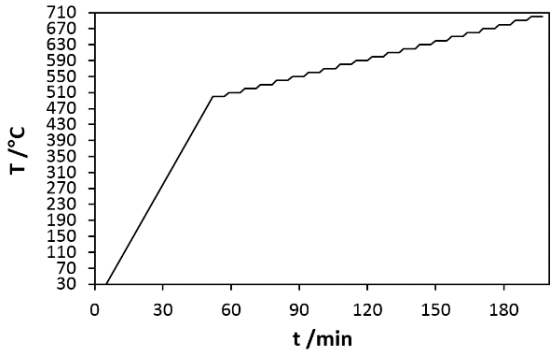


**Fig. S2** Temperature vs. time curve for the 30 °C- 700 °C *in situ* temperature-dependent experiments. Data were taken for 5 min starting from 30 °C at each 10 °C in the 500-700 °C interval where the heating rate was kept constant at 10 °C·min$^{-1}$

### *In situ* XRD experiments

*In situ* temperature-dependent XRD experiments were performed using Reactor X reaction environment attached to Rigaku SmartLab diffractometer equipped with a rotating anode (9 kW, 45 kV, 200 mA) operated in the Bragg–Brentano geometry (Cu K$\alpha_{1,2}$: 1.541862 Å). The powder sample was placed on a silicon sample holder, which was heated from 30 °C to 700 °C at 10 °C·min$^{-1}$ heating rate by infrared radiation under continuous flow of synthetic air at a rate of 20 mL·min$^{-1}$. Data were collected at each 10 °C between 500 - 700 °C and at 30 °C before and after the heating experiment in the 10 - 60°2θ range at a scan rate of 5° ·min$^{-1}$ (step size, 0.01°) with a HyPix-3000 multidimensional detector (one-dimensional mode).

### Characterization

*Ex situ* powder patterns were collected on a STOE StadiP transmission diffractometer (MoK$\alpha_1$). The diffractometer is equipped with a primary monochromator (Germanium (111) and a solid-state detector (Mythen 1K). The sample was prepared in a glass capillary with an inner diameter of 0.5 mm.

The specific surface area was determined by nitrogen sorption experiments with a Quantachrome NOVA 3200e instrument after degassing approximately 150 mg powder samples at 150 °C

overnight. Data were evaluated by the BET (Brunauer-Emmett-Teller) method using the adsorption data in the relative pressure range of 0.05 to 0.2. From the specific surface area, approximate particle sizes can be calculated using the relation $D_p = 6000 \cdot \sigma^{-1} \cdot A_s^{-1}$ (assuming spherical particles, $D_p$ = particle size in nm, σ = specific density in $g \cdot cm^{-3}$, $A_s$ = specific surface area $m^2 \cdot g^{-1}$). Dynamic light scattering (DLS) data were collected from the powder redispersed in the water-methanol mixture. The suspension obtained in this way was ultrasonicated for 30 min. The data were recorded on a Malvern Zetasizer Nano-ZS using laser radiation with a wavelength of 633 nm. The scattered light was measured at a backscattering angle of 173 °.

Thermogravimetry (TG) and differential scanning calorimetry (DSC) measurements were carried out using a NETZSCH STA 449 F3 Jupiter thermal analyzer for the qualitative analysis of crystallization temperatures. The measurements were carried out under an air flow of 40 $mL \cdot min^{-1}$ using approximately 10 mg powder heated in an aluminum oxide crucible with heating rates of 2, 5 and 10 $°C \cdot min^{-1}$.

Fourier transform infrared (FTIR) spectroscopy measurements were performed using a Perkin Elmer Spectrum Two spectrometer with an attenuated total reflectance (ATR) unit. For construction of the clusters Avogadro molecular editor[6] and for visualization of the structures Diamond software[7] is used.

Scanning transmission electron microscopy (STEM) imaging was performed using a Titan Themis microscope (Thermo Fisher Scientific) operated at 300 kV. Aberration correction of the probe forming lens allows for a convergence angle of 24 mrad, corresponding to a probe size of 0.1 nm. Annular bright field (ABF) and high angle annular dark field (HAADF) images were collected using corresponding detectors with the angular range of 8–16 mrad and 73–200 mrad, respectively.

STEM-EDS spectrum imaging was acquired using the SuperX detector. Multivariate statistical analysis was performed on the datasets to reduce the noise and highlight the spatial variation of EDS signals from different elements.[8]

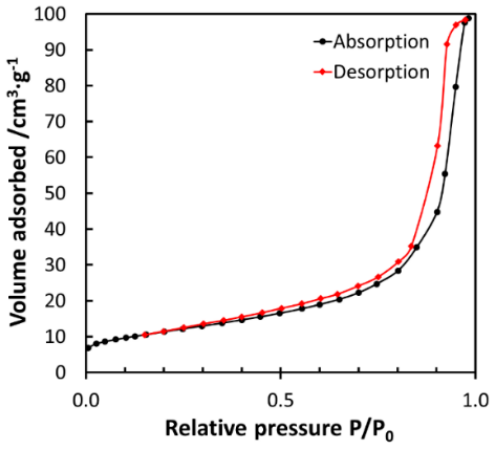


**Fig. S3** Nitrogen adsorption/desorption isotherms after degassing approximately 110 mg powder at 150 °C overnight (15.3 wt% loss).

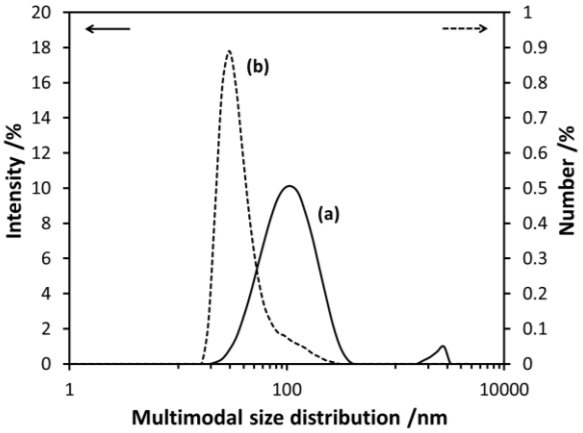


**Fig. S4** Results of the dynamic light scattering obtained (a) after centrifugation and ultrasonication and (b) after filtering. Solid lines show the intensity percentage while dashed lines show the number percentage of the particles (Note that the x-axis on a logarithmic scale).

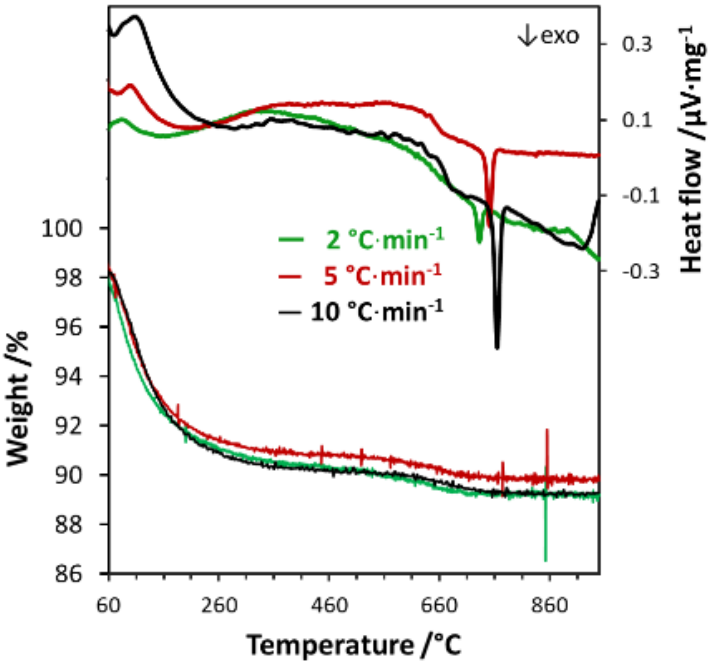


**Fig. S5** (a) Differential scanning calorimetry (DSC) and thermogravimetric (TG) data obtained from $Na_xTa_yO_z$ and (b) features of the DSC peaks measured with heating rates 2 °C·min$^{-1}$ (green), 5 °C·min$^{-1}$ (red) and 10 °C·min$^{-1}$ (black) in air.

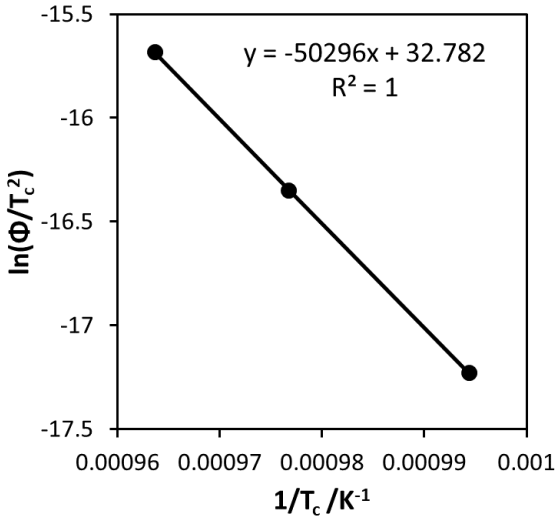


**Fig. S6** Kissinger plot from DSC data. The activation energy is calculated from the slope as $E_a$ = -47701*8.314 J·K$^{-1}$·mol$^{-1}$ = 396586 J·K$^{-1}$·mol$^{-1}$ = 418 kJ·K$^{-1}$·mol$^{-1}$.

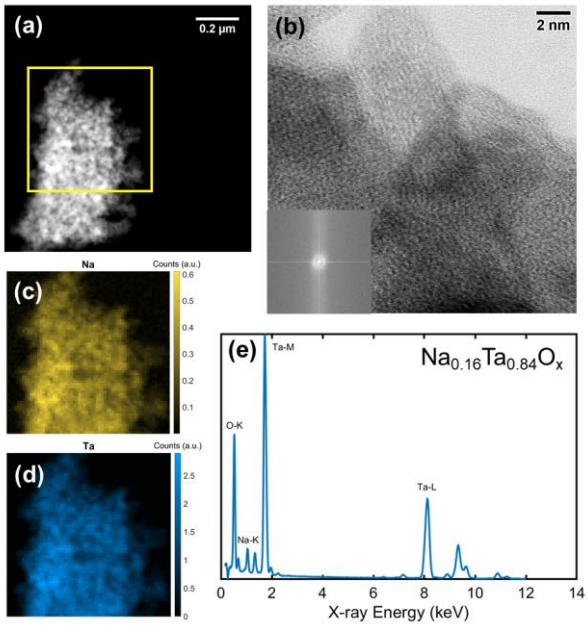


**Fig. S7** (a) HAADF-STEM image of the amorphous material $Na_xTa_yO_z$. (b) Respective ABF image and corresponding FFT pattern (inset). Spatial distribution of (c) Na and (d) Ta elements and (d) composition obtained by STEM-EDS spectrum. Data analysis of the EDS maps is done according to[8].

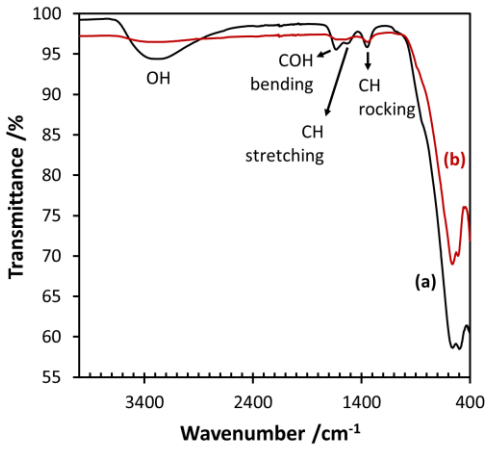


**Fig. S8** FTIR spectra obtained using ATR mode from (a) as-prepared $Na_xTa_yO_z$ sample and (b) the sample obtained after calcining at 700 °C $Na_xTa_yO_z$-700.

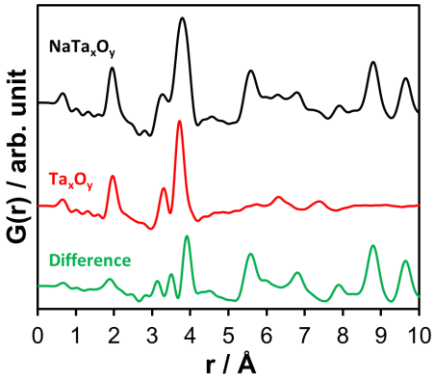


**Fig. S9** The difference PDF obtained by subtracting the PDF obtained from the amorphous non-heat treated material from that obtained for the heat-treated material. Note that the intensity of the functions are normalized to that of the most intense peak.

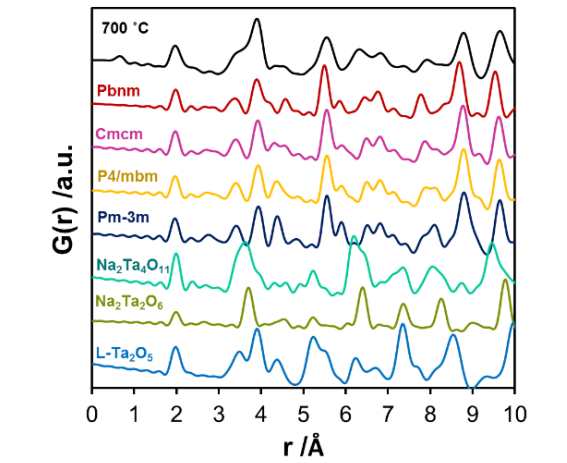


**Fig. S10** PDFs simulated using the natrotantite ($Na_2Ta_4O_{11}$),[9] tantalum pentoxide ($L\text{-}Ta_2O_5$)[10] and perovskite ($NaTaO_3$) structure models[11] in *Pbnm*, *Cmcm*, *P4/mbm* and $Pm\bar{3}m$ space groups compared to the PDF obtained from the experimental data collected at 700 °C. Refinements with the inclusion of pyrochlore phase ($Na_2Ta_2O_6$)[11] was observed not to give a reasonable fit result.

a)

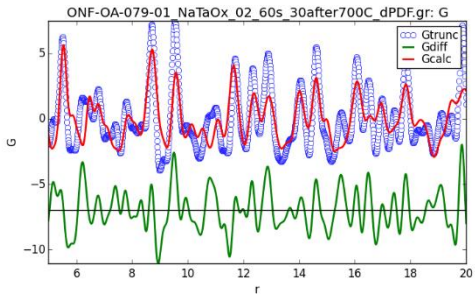


b)

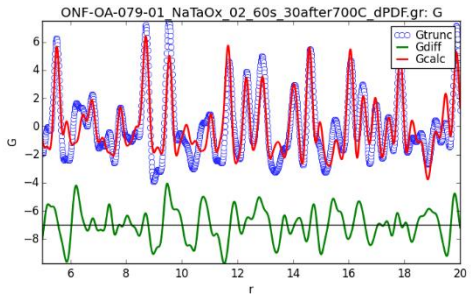


**Fig. S11** Fit to the difference PDF (5-20 Å) using a) $NaTaO_3$-*Cmcm* (Rw-value: 0.66) and b) $NaTaO_3$-*Pbnm* (Rw-value: 0.48) structure models.

a)

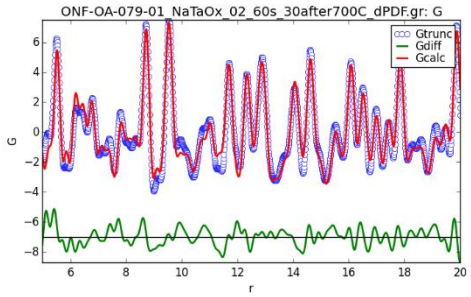


b)

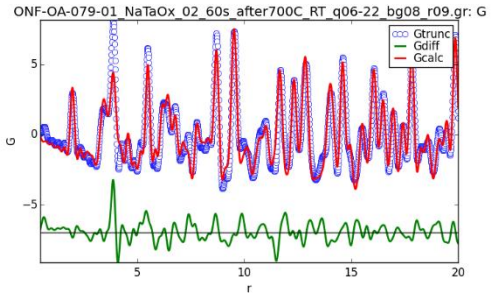


**Fig. S12** (a) Fit to the difference PDF (5-20 Å) using $NaTaO_3$-*Pbnm* and $Na_2Ta_4O_{11}$ structure models (Rw-value: 0.25). The results give 57:43 ratio of $NaTaO_3$-*Pbnm* and $Na_2Ta_4O_{11}$ in terms of weight. (b) Fit to the PDF (0-20 Å) (Rw-value: 0.29) obtained at ambient temperature from the heat-treated material using $Na_2Ta_4O_{11}$[9] and $NaTaO_3$-*Pbnm*[10] structure models.

**Table S1** Results of the refinement of the first 20 Å range of the PDF obtained from the heat-treated material with error values given in parentheses (Rw-value: 0.24).

| | | $NaTaO_3$-*Pbnm* | | $Na_2Ta_4O_{11}$ | | L-$Ta_2O_5$ | |
|---|---|---|---|---|---|---|---|
| Parameter | | Initial | Refined | Initial | Refined | Initial | Refined |
| Scale factor | | 1 | 0.329726 (0.004) | 1 | 0.33863 (0.016) | 1 | 0.12079 (0.008) |
| Lattice parameters /Å | | | | | | | |
| | a | 5.4768 | 5.51315 (0.002) | 6.2092 | 6.20423 (0.003) | 6.198 | 6.21274 (0.020) |
| | b | 5.5212 | 5.52606 (0.002) | 6.2092 | 6.20423 (0.003) | 40.29 | 40.8566 (0.130) |
| | c | 7.789 | 7.78164 (0.002) | 36.619 | 36.7057 (0.019) | 3.888 | 3.84649 (0.007) |
| Quadratic corr. factor | | 1 | 0.074727 (0.520) | 1 | 0.35413 (1.5) | 1 | 1.0033 (2.7) |
| Linear corr. factor | | 1 | 1.5504 (0.140) | 1 | 0.24173 (0.4) | 1 | 3.35879 (0.630) |
| Particle diameter /Å | | - | - | 80 | 201.4 (46) | - | |
| Low r sigma ratio | | 1 | 1.12409 (0.012) | 1 | - | 1 | 1.15839 (0.150) |
| R cutoff /Å | | 70 | - | - | - | 15 | - |
| $U_{xx}$ /Å$^2$ | | | | | | | |
| | Na | 0.005 | 0.005212 (0.002) | 0.005 | 0.00621 (0.003) | - | - |
| | Ta | 0.005 | 0.004181 (0.001) | 0.005 | 0.0046 (0.001) | 0.005 | 0.0076 (0.002) |
| | O | 0.005 | 0.005245 (0.006) | 0.005 | 0.00817 (0.002) | 0.005 | 0.00457 (0.011) |
| Phase fraction /at% | | | 0.476427 (0.010) | | 0.40825 (0.012) | | 0.11533 (0.007) |
| Phase fraction /wt% | | | 0.444567 (0.010) | | 0.42061 (0.012) | | 0.13483 (0.008) |

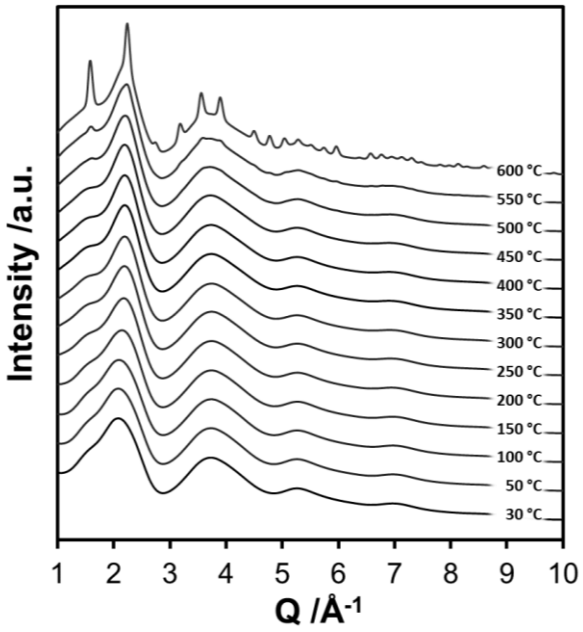


**Fig. S13** X-ray total scattering patterns obtained from the first set of *in situ* heating experiments performed between 30-600 °C with 50 °C intervals above 50 °C.

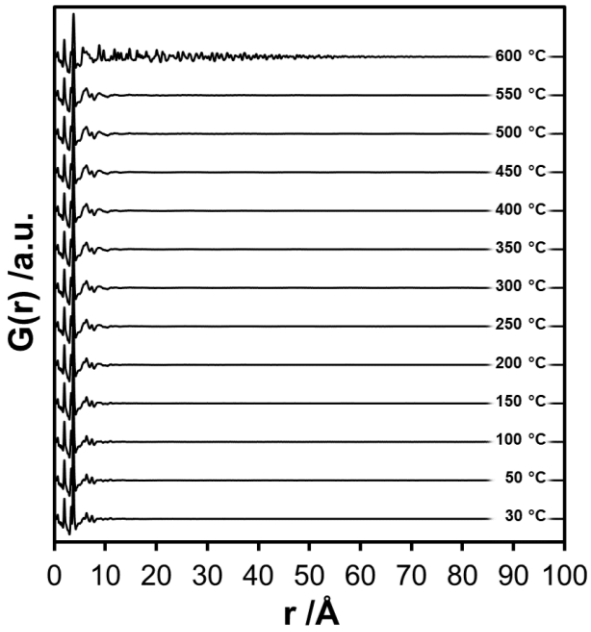


**Fig. S14** 100 Å-PDFs obtained from the first set of *in situ* heating experiments indicating substantial changes in the local structure between 550-600 °C.

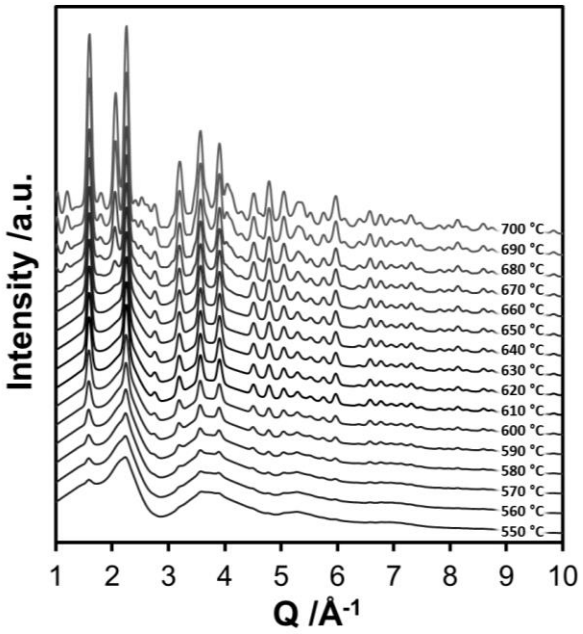


**Fig. S15** Total scattering patterns obtained from the second set of *in situ* heating experiments performed between 30-700 °C with 10 °C intervals above 550 °C.

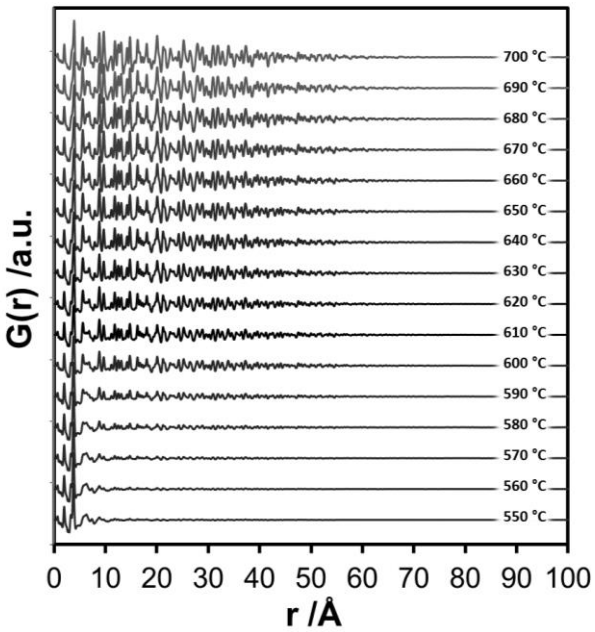


**Fig. S16** 100 Å-PDFs obtained from the second set of *in situ* heating experiments between 550-700 °C displaying the evolution of the local structure.

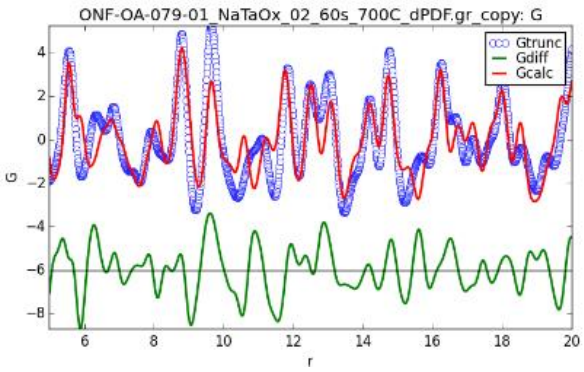


**Fig. S17** Fit to the 700 °C dPDF using $NaTaO_3$-*Pm*$\bar{3}$*m* structure model (Rw: 0.57).

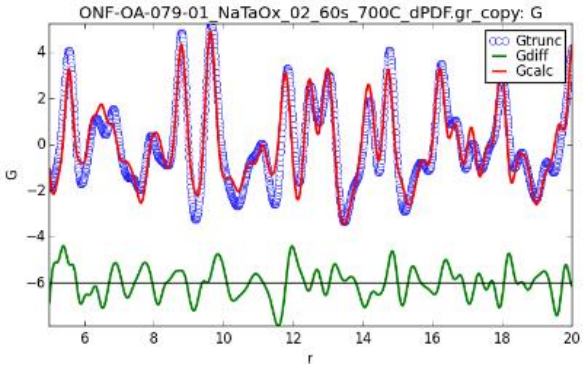


**Fig. S18** Fit to the 700 °C dPDF using $NaTaO_3$-*Pm*$\bar{3}$*m* and $Na_2Ta_4O_{11}$ structure models (Rw: 0.36).

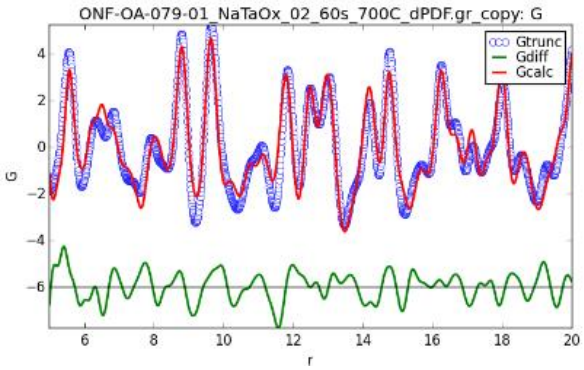


**Fig. S19** Fit to the 700 °C dPDF using $NaTaO_3$-*P4/mbm* and $Na_2Ta_4O_{11}$ structure models (Rw: 0.33).

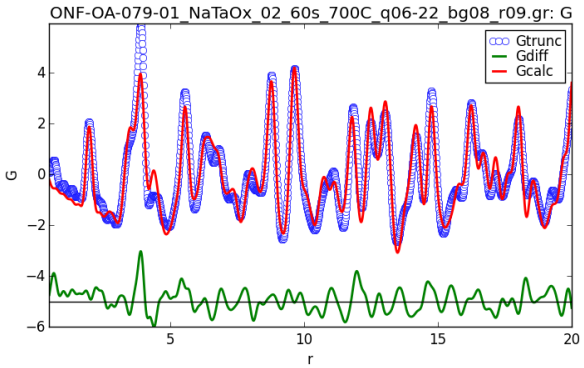


**Fig. S20** Fit to the 700 °C PDF using $NaTaO_3$-*P4/mbm*, $Na_2Ta_4O_{11}$ and L-$Ta_2O_5$ structure models (Rw: 0.29).

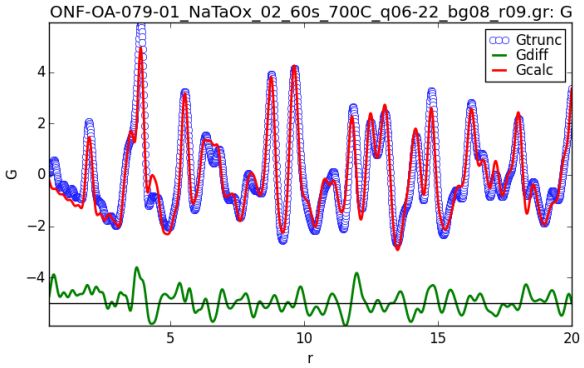


**Fig. S21** Fit to the 700 °C PDF using $Na_2Ta_4O_{11}$, L-$Ta_2O_5$, $NaTaO_3$-*P4/mbm* and $NaTaO_3$-*Cmcm* structure models (Rw: 0.26).

a)

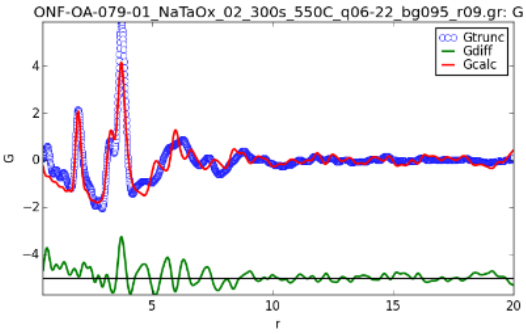


b)

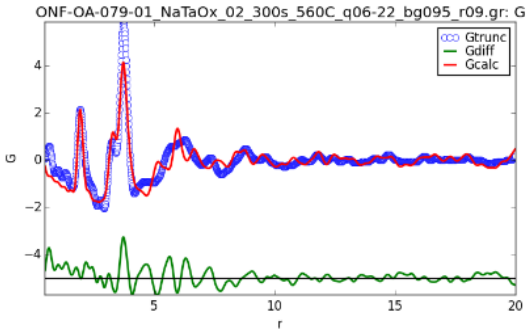


c)

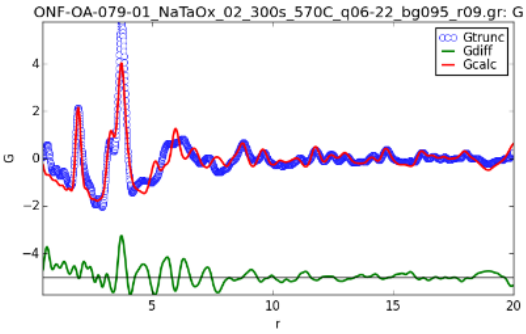


d)

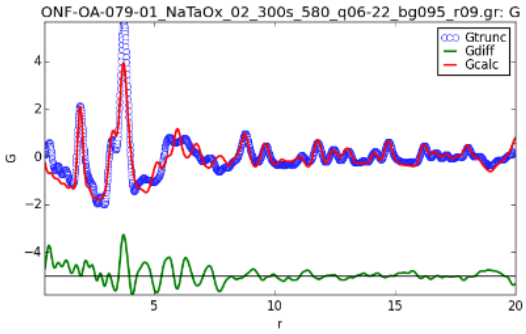


e)

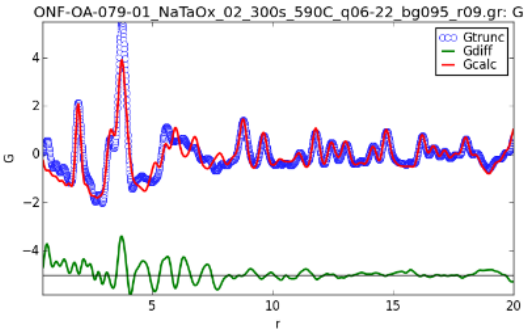


f)

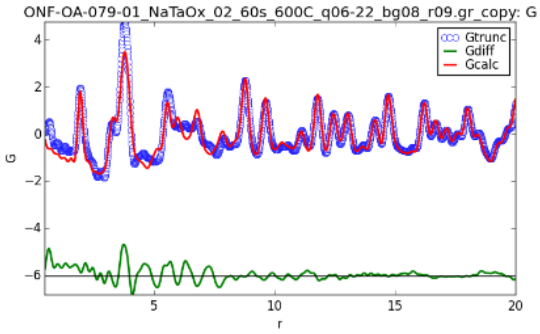


g)

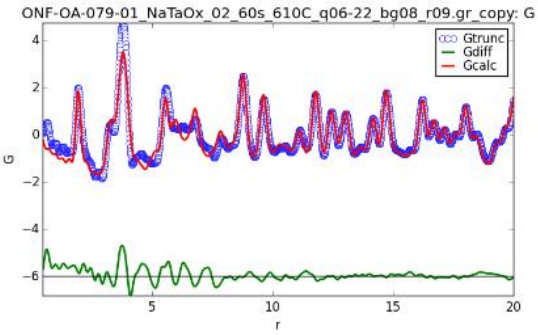


h)

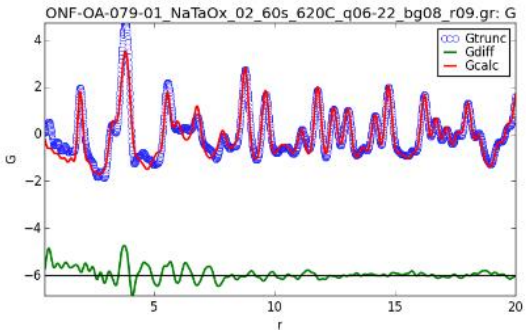


*continued*

k)

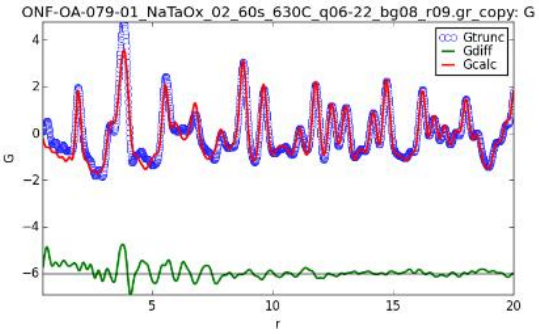


l)

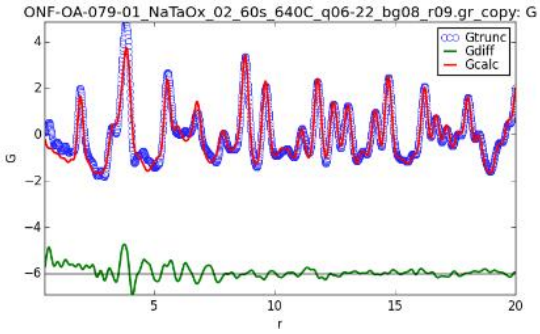


m)

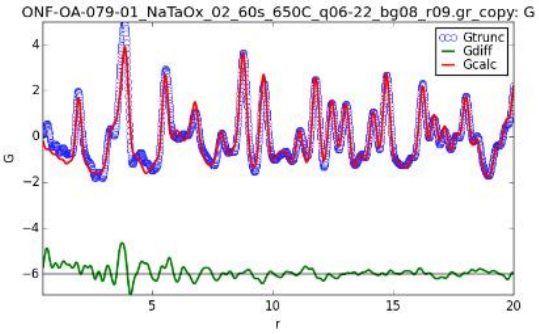


n)

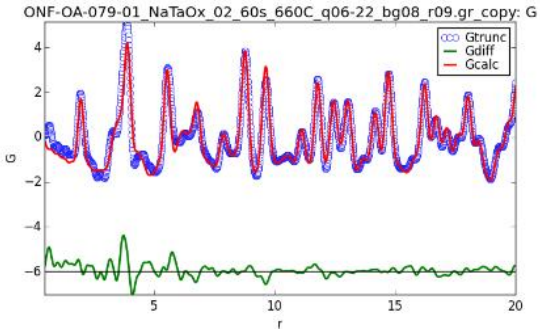


o)

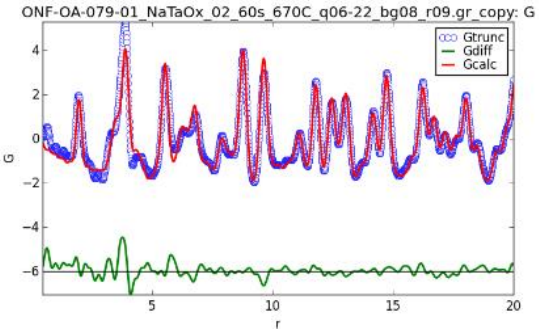


p)

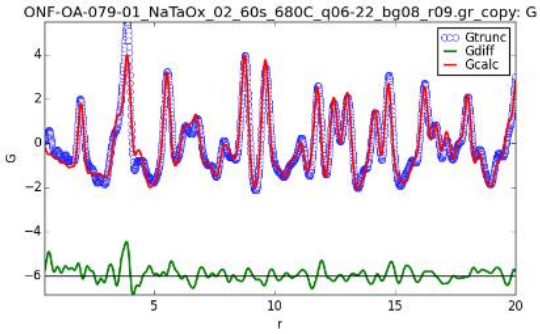


r)

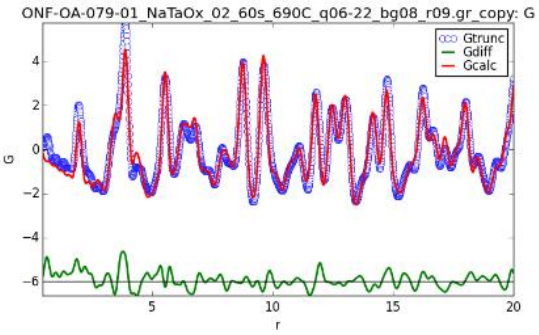


s)

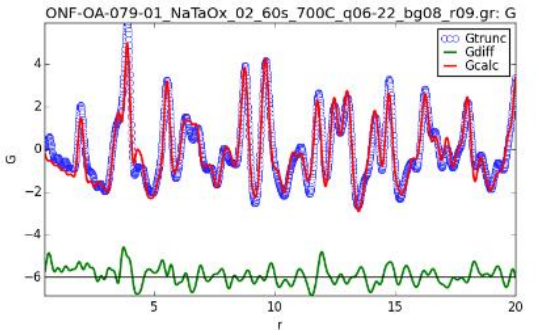


*continued*

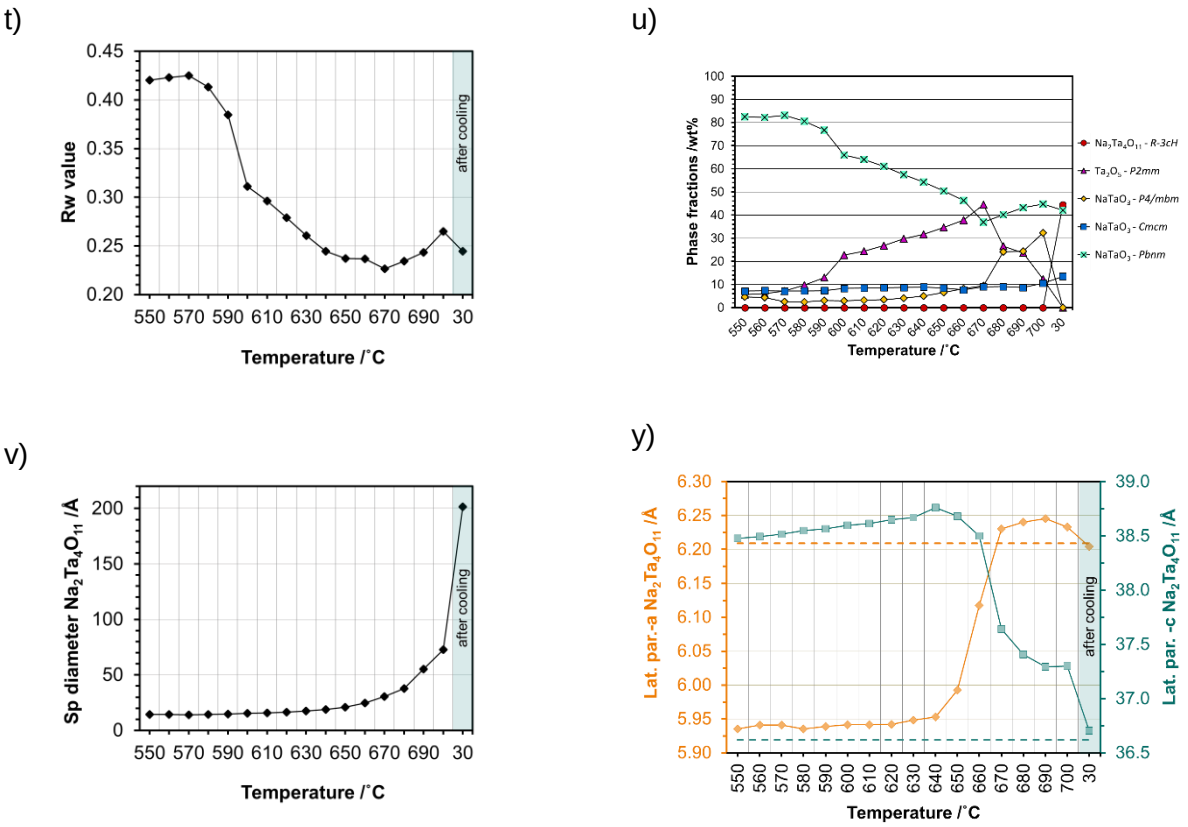


**Fig. S22** (a-s) Refinements of the 550-700 °C PDFs using $Na_2Ta_4O_{11}$, $NaTaO_3$-*P4/mbm*, $NaTaO_3$-*Cmcm* and L-$Ta_2O_5$ structure models. (t) Plot of the Rw-values vs. the temperatures that the data is collected at. (u) Plot of the phase fractions (wt%) vs. temperature. (v) Plot of the change of the crystallite size and (y) lattice parameters calculated for $Na_2Ta_4O_{11}$ phase vs. temperature. Note that the dashed lines in (y) show the lattice parameter values obtained from the model structures.

**Table S2** Phase fractions in terms of at% calculated based on the refinements of the first 20 Å range of the PDFs obtained from the data at different temperatures together with the calculated error values

| T /˚C | $NaTaO_3$ (Pbnm) | ± | $NaTaO_3$ (Cmcm) | ± | $NaTaO_3$ (P4/mbm) | ± | $Na_2Ta_4O_{11}$ ($R\bar{3}cH$) | ± | L-$Ta_2O_5$ (P2mm) | ± |
|---|---|---|---|---|---|---|---|---|---|---|
| **550** | 0.0 | 0.0 | 6.3 | 1.1 | 5.1 | 1.0 | 82.3 | 1.7 | 6.3 | 1.2 |
| **560** | 0.0 | 0.0 | 6.7 | 1.1 | 4.8 | 0.9 | 82.0 | 1.8 | 6.5 | 1.2 |
| **570** | 0.0 | 0.0 | 7.9 | 1.2 | 2.9 | 1.1 | 83.0 | 2.0 | 6.3 | 1.3 |
| **580** | 0.0 | 0.0 | 10.8 | 1.3 | 2.8 | 1.1 | 80.2 | 2.0 | 6.3 | 1.3 |
| **590** | 0.0 | 0.0 | 14.2 | 1.1 | 3.3 | 1.1 | 76.0 | 1.7 | 6.5 | 1.2 |
| **600** | 0.0 | 0.0 | 24.7 | 1.3 | 3.2 | 1.1 | 64.9 | 1.9 | 7.2 | 1.4 |
| **610** | 0.0 | 0.0 | 26.4 | 1.6 | 3.5 | 1.3 | 62.8 | 2.0 | 7.3 | 1.5 |
| **620** | 0.0 | 0.0 | 29.0 | 1.9 | 3.7 | 1.6 | 59.8 | 2.2 | 7.5 | 1.5 |
| **630** | 0.0 | 0.0 | 32.1 | 2.0 | 4.4 | 1.7 | 56.0 | 2.3 | 7.5 | 1.4 |
| **640** | 0.0 | 0.0 | 34.1 | 2.0 | 5.5 | 1.6 | 52.8 | 2.2 | 7.6 | 1.4 |
| **650** | 0.0 | 0.0 | 37.0 | 2.2 | 7.0 | 1.8 | 48.8 | 2.3 | 7.2 | 1.3 |
| **660** | 0.0 | 0.0 | 40.2 | 2.1 | 8.8 | 1.7 | 44.5 | 2.2 | 6.5 | 1.2 |
| **670** | 0.0 | 0.0 | 47.1 | 1.9 | 10.0 | 1.5 | 35.4 | 1.8 | 7.5 | 1.2 |
| **680** | 0.0 | 0.0 | 28.1 | 1.8 | 25.6 | 1.5 | 38.6 | 2.1 | 7.7 | 1.1 |
| **690** | 0.0 | 0.0 | 25.1 | 1.7 | 25.9 | 1.3 | 41.6 | 1.5 | 7.4 | 0.9 |
| **700** | 0.0 | 0.0 | 13.1 | 1.4 | 34.6 | 1.1 | 43.3 | 1.2 | 9.0 | 0.8 |
| **30** | 47.7 | 1.0 | 0.0 | 0.0 | 0.0 | 0.0 | 40.8 | 1.2 | 11.5 | 0.7 |

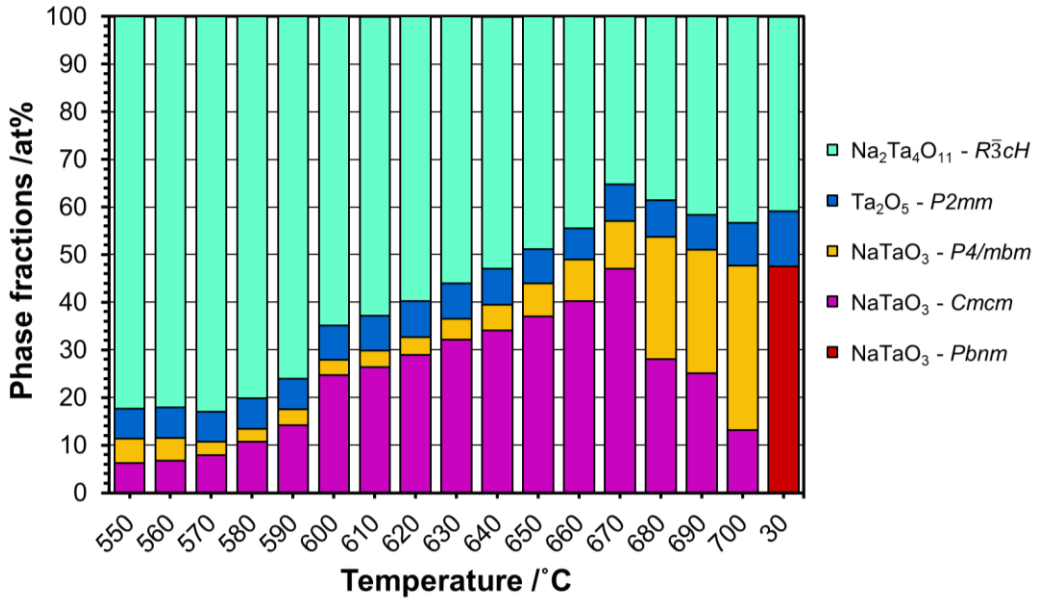


**Fig. S23** Phase fractions in terms of at% calculated based on the refinements of the first 20 Å range of the PDFs obtained from the scattering data collected during heating from 550 °C to 700 °C, together with the *ex situ* results after cooling.

a)

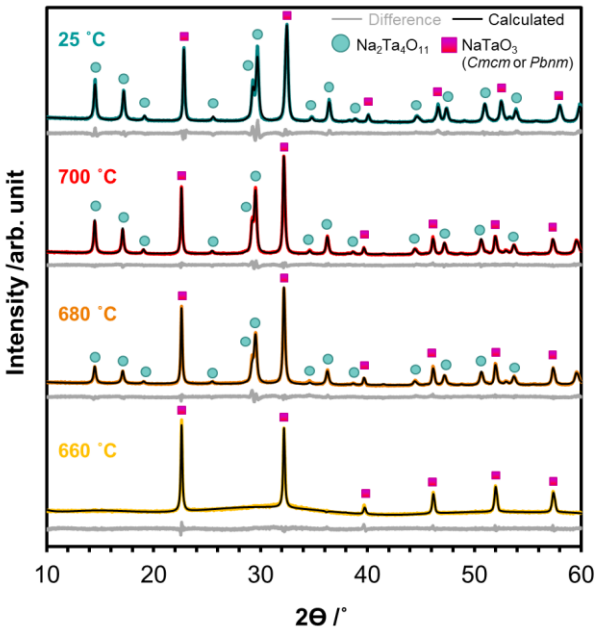


b)

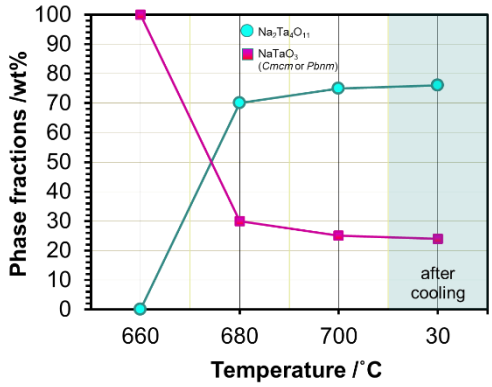


**Fig. S24** (a) Rietveld refinements of the *in situ* XRD patterns obtained at 660, 680, 700 °C and at 25 °C after cooling down, using $Na_2Ta_4O_{11}$ and $NaTaO_3$ structure models. (b) Plot of the fractions of natrotantite and perovskite phases. Note that refinements using $NaTaO_3$ with *Cmcm* and Pbnm space groups give the same result of the phase fractions.

## References


1. T. Grewe and H. Tüysüz, *ACS Appl Mater Interfaces*, 2015, **7**, 23153-23162.
2. J. Filik, A. W. Ashton, P. C. Y. Chang, P. A. Chater, S. J. Day, M. Drakopoulos, M. W. Gerring, M. L. Hart, O. V. Magdysyuk, S. Michalik, A. Smith, C. C. Tang, N. J. Terrill, M. T. Wharmby and H. Wilhelm, *J Appl Crystallogr*, 2017, **50**, 959-966.
3. P. Juhás, T. Davis, C. L. Farrow and S. J. L. Billinge, *Journal of Applied Crystallography*, 2013, **46**, 560-566.
4. X. Yang, P. Juhas, C. L. Farrow and S. J. L. Billinge, *Journal of Applied Crystallography*, 2014, DOI: 10.48550/arXiv.1402.3163.
5. C. L. Farrow, P. Juhas, J. W. Liu, D. Bryndin, E. S. Bozin, J. Bloch, T. Proffen and S. J. Billinge, *J Phys Condens Matter*, 2007, **19**, 335219.
6. M. D. Hanwell, D. E. Curtis, D. C. Lonie, T. Vandermeersch, E. Zurek and G. R. Hutchison, *J Cheminform*, 2012, **4**, 17.
7. K.Brandenburg and H.Putz, DIAMOND (Version 3.2k), Crystal Impact GbR, Bonn, Germany, 2005.
8. S. Zhang and C. Scheu, *Microscopy*, 2018, **67**, i133-i141.
9. T. S. Ercit, F. C. Hawthorne and P. Cerny, *Bulletin De Mineralogie*, 1985, **108**, 541-549.
10. N. C. Stephenson and R. S. Roth, *Acta Crystallographica Section B Structural Crystallography and Crystal Chemistry*, 1971, **27**, 1037-1044.
11. B. J. Kennedy, A. K. Prodjosantoso and C. J. Howard, *Journal of Physics-Condensed Matter*, 1999, **11**, 6319-6327.